A novel synergistic enzyme-Antibiotic Therapy with Immobilization of Mycobacteriophage LysinB enzyme onto Rif@UiO-66 Nanocomposite for Enhanced Anti-TB Nanotherapeutic; Nanoenzybiotics approach

Zienab E. Eldin (t-zienabessam@zewailcity.edu.e.g)
Beni-Suef University
Tarek Dishisha
Beni- Suef University
Ossama M. Sayed
Sinai University—Kantara Branch
Hanaa. M. Salam
Port Said University
Ahmed. Farghali
Beni-Suef University

Research Article

Keywords: Mycobacteriophage D29 Lysin B enzyme, Metal-organic framework, Rifampicin, Enzyme-antibiotic combination, Cytotoxicity, Biodistribution

Posted Date: August 23rd, 2023

DOI: https://doi.org/10.21203/rs.3.rs-3274529/v1

Abstract

The emergence of antibiotic-resistant and phage-resistant strains of Mycobacterium tuberculosis (M. tuberculosis) necessitates improving new therapeutic plans. The objective of the current work was to ensure the effectiveness of rifampin and the mycobacteriophage LysB D29 enzyme in the treatment of MDR-TB infection, where new and safe metal–organic framework (MOF) nanoparticles were used in combination. UiO-66 nanoparticles were synthesized under mild conditions in which the antimycobacterial agent (rifimpacin) was loaded (Rif@UiO-66) and LysB D29 enzyme immobilized onto Rif@UiO-66, which were further characterized. Subsequently, the antibacterial activity of different ratios of Rif@UiO-66 and LysB/Rif@uio-66 against the nonpathogenic tuberculosis model Mycobacterium smegmatis (M. smegmatis) was evaluated by minimum inhibitory concentration (MIC) tests. Impressively, the MIC of LysB/Rif@uio-66 was 16-fold lower than that of pure rifampicin. In vitro and in vivo toxicity studies proved that LysB/Rif@UiO-66 is a highly biocompatible therapy for pulmonary infection. A biodistribution assay showed that LysB/Rif@UiO-66 showed a 5.31-fold higher drug concentration in the lungs than free rifampicin. A synergistic interaction between UiO-66, rifampicin and the mycobacteriophage lysB D29 enzyme was shown in the computational method (docking). Therefore, all results indicated that the LysB/Rif@UiO-66 nanocomposite exhibited promising innovative enzyme-antibiotic therapy for tuberculosis treatment.

1. Introduction

Mycobacterium tuberculosis (Mtb) is a highly pathogenic microorganism that mostly affects the lungs and other tissues and causes the infectious illness known as tuberculosis (TB), which is communicable and results in the typical syndromes of pulmonary and extra pulmonary infection [1]. In 2020, 10 million persons had the active form of tuberculosis (ATB), according to the World Health Organization's (WHO) Global TB Report 2021 [2], and approximately 25% of the world's population had immunologic evidence of a former *Mtb* infection as established by surveillance tests. This infectious bacteria following COVID-19 is the second-leading cause of mortality worldwide [2–4]. M. smegmatis is a nonpathogenic relative of M. tuberculosis and is widely used as a pulmonary model to screen TB drugs [5, 6]. For more than 50 years, antibiotics have been administered to manage TB, but the disease's long-term multidrug requirements and stringent adherence to treatment are significant barriers to effective therapy. Since this medication is administered for a lengthy period of time, patients have a significant likelihood of stopping the medication before the bacteria have been entirely eradicated, which undermines the patient's compliance and adherence to therapy [7, 8]. There are limited options to treat resistant TB infections that develop through the development of a cell wall permeability barrier and toxicity due to long-term antibiotic therapy, which leads to resistance and incompliance [9, 10].

The majority of gram-positive and some gram-negative bacteria are both sensitive to the hydrophobic antibiotic rifampicin (Rif); the bactericidal effect is achieved by impeding gene expression by regulating DNA synthesis. Rif has restricted usage due to its several disadvantages, including its poor dissolution, low absorption, and liver toxicity [11, 12]. Combining phages with already available antibiotics might enhance the effectiveness of the antibiotic against multidrug-resistant bacteria by extending or even restoring their action against particular bacteria [13, 14].

The mycobacteriophage D29 LysinB enzyme has been applied prophylactically to prevent M. tuberculosis infection in many animal models [15, 16]. Purified Lysin B enzyme from Mycobacteriophage D29 has been demonstrated to induce extracellular lysis and remove biofilms [17]. It works by splitting the particular ester that connects the arabinogalactan and mycolic acid-rich outer membrane, unleashing free mycolic acids and leading to cell death [18]. There is an emerging trend to apply metal organic frameworks [MOFs], which are a versatile class of hybrid materials composed of metal-based clusters connected in three dimensions by organic linkers, in drug delivery due to their excellent characteristics [19, 20]. The current work aimed to prepare novel UiO-66 nanoparticles as carriers for Rif and immobilization of LysB to improve enzyme-antibiotic therapy toward pulmonary-resistant Mycobacterium tuberculosis.

2. Experimental section

2.1 Materials

2.1.1 Chemicals

Zirconium chloride ($ZrCl_4$) (99.5%), 1,4-benzenedicarboxylic acid (H2BDC) (99%), and polyvinylpyrrolidone (PVP) (95%) were purchased from Chem-Lab (Belgium). Rifampicin 99% and *p*-nitrophenyl palmitate (*p*NPP; C16) were procured from Sigma—Aldrich (USA), while N,N-dimethylformamide (DMF) (99.5%), glacial acetic acid and dimethyl sulfoxide (DMSO) (99%) were supplied by Merck KGaA (Germany).

2.1.2. Bacterial strain, culture media and kits

Mycobacterium smegmatis mc2155 (ATCC 700084) was used in the present study as a model microorganism. It was purchased from the American Type Culture Collection (ATCC) (Manassas, VA, USA) and grown in Mueller-Hinton agar (MHA) containing, per liter, 2.0 g of meat infusion, 17.5 g of casein hydrolysate, 1.5 g of starch and 13.0 g of agar—agar (pH 7.4 ± 0.2) (Merck, Germany). A lactate dehydrogenase (LDH) assay kit (ab102526) was purchased from Abcam (USA). A BCA protein quantification kit (20201ES76) was purchased from China.

2.1.3. Cloning, Expression and Purification of LysB-His6Enzymes (LysB-D29)

According to different reports [21, 22], the encoded form LysB-His6 gBlocks were cloned and generated, and the recombinant LysB-D29 enzyme was isolated. The isolated enzyme was kept at -20°C after being freeze dried (Christ Alpha 1–4 Frost-Dryer, Beni-Suef University, Beni-Suef, Egypt).

2.2. UiO-66 metal organic framework (MOF) synthesis

The synthesis of UiO-66 was conducted following a solvothermal strategy as reported earlier in Li et al. [23] with slight modifications. Briefly, a mixture of $ZrCl_4$ (0.53 g) and H2BDC (0.35 g) was dissolved in 100 mL of DMF at room temperature. Subsequently, 3.5 mL of acetic acid was added, and the resulting mixture was transferred into a Teflon-lined stainless-steel tube that was autoclaved at 121°C for 24 h. After cooling the resulting mixture at room temperature, centrifugation was performed (6000× g, 15 min, 4°C; Thermo Scientific, Waltham, MA, USA) to collect the white precipitate of UiO-66. The precipitate was washed three times with DMF and then dried at 150°C overnight.

2.3. Rif@UiO-66 nanocomposite synthesis

The synthesis of rifampicin-loaded Uio-66 was performed as reported previously by Ahmed et al. [24] with some modifications. Rif was dissolved in DMSO until reaching a final concentration of 15 mg/mL. Subsequently, 100 mg of UiO-66 was added and dispersed into the solution. The resulting suspension was stirred for three days at room temperature. Finally, the sample was filtered, washed with DMSO and then with distilled water to eliminate unabsorbed Rif on UiO-66 and then dried at 60°C overnight.

2.4. Immobilization of Lysin B mycobacterioPhage D29 onto Rif@UiO-66

A physical adsorption technique was employed for immobilization of Lysin B mycobacteriophage D29 onto Rif@UiO-66. A total of 20 mg Rif@UiO-66 was incubated overnight with 3 mL (0.5 mg/mL) of Lysin B at 4°C on a rocking table for 48 h [25]. Rif@UiO-66 with bound Lysin B was collected by centrifugation (5000× g, 15 min, 4°C; Thermo Scientific, Waltham, MA, USA) followed by 3 repeated washes (15 min each) to eradicate any unbound enzyme and then stored at 4°C for further assays.

2.5. Characterization

2.5.1. X-ray diffraction (XRD)

XRD patterns were determined using a PANalytical (Empyrean) X-ray diffractometer system at 40 kV and 35 mA with monochromatized Cu Kα radiation (λ = 1.5406 Å) and a scanning speed of 2 per min (step size = 0.050 and step time = 1.5 s). The scanning range (2θ scale) was within 5–80.

2.5.2. Fourier transform infrared spectrometry (FTIR)

FTIR (4000 – 500 cm^{-1}) was acquired by Vertex 70 (Bruker, Germany) in a KBr pellet to predict the functional groups of the prepared samples. The resolution used in the scans was 1 cm^{-1}, and the spectra were averaged over three scans.

2.5.3. Thermal stability

The thermal stability of UiO-66 MOFs and the RiF@UiO-66 nanocomposite was investigated by thermogravimetric analysis using Perkin-Elmer Pyris (TGA) (Massachusetts, USA) and a heating rate of 10°C per min ranging from 50–600°C under a nitrogen atmosphere.

2.5.4. Surface area, pore volume and pore size (BET)

The specific surface areas were determined using the Brunauer–Emmett–Teller (BET) method. Theory using N_2 adsorption-desorption isotherm (Quantachrome TouchWin Software version 1.21) at 77 K after degassing at 150°C under vacuum for 3 h. The pore volume and pore size distribution were calculated according to the Barrett–Joyner–Halenda theory (BJH).

2.5.5. Zeta potential and hydrodynamic particle size measurements

The mean hydrodynamic size, particle size distribution, and polydispersity were measured by the dynamic light scattering (DLS) method using a ZS90 Zetasizer instrument (Malvern, UK). The zeta potential, which reflects the colloidal stability, was determined by electrophoretic laser Doppler velocimetry.

2.5.6 High-resolution transmission electron microscopy (HRTEM) and field emission scanning electron microscopy (FESEM)

To evaluate the surface morphology and particle size of the prepared sample, Rif@UiO-66 was investigated by high-resolution transmission electron microscopy (HRTEM) using a JEOL JEM-2100 operated at 200 kV. Additionally, scanning electron microscopy (SEM) analysis was performed with a field emission scanning electron microscope (FESEM) using a Philips-XL30 device (The Netherlands) equipped with energy-dispersive X-ray (EDX) microanalysis hardware.

2.6. Determination of loading capacity and entrapment efficiency

After loading Rif into UiO-66, the suspensions were centrifuged at 15000× g for 20 min at 4°C (Thermo Scientific, Waltham, MA, USA) to separate the supernatant phase containing the free unbound Rif. The concentration was determined using a UV/Vis spectrophotometer (Thermo Scientific Evolution 600, USA) at λmax = 400 nm. The absorbance was used to calculate the entrapment efficiency (EE) and loading capacity (LC) of Rif to UiO-66 nanoparticles using the following equations as described in [26, 27]:

$$\mathrm{EE}\,(\%) = \frac{\mathrm{RiFweightinnanoparticles}}{\mathrm{weightofRiFfedinitially}} * 100$$

Eq. (A.1)

$$\mathrm{LC}\,(\%) = \frac{\mathrm{RiFweightinsample}}{\mathrm{totalweightofsample}} * 100$$

Eq. (A.2)

2.7. Immobilization yield and binding capacity assays

The immobilization yield (IY) was determined from the variance among the initial enzyme level in solution prior to immobilization and the residual enzyme level in the supernatant and washings prior to immobilization. The enzyme content was estimated using the BCA procedure [28].

The immobilization yield was determined as follows:

$$\mathrm{IY\%} = \frac{\mathrm{amtofenzymebeforeimmobilization} - \mathrm{amtofresidulenzymeafterimmobilization}}{\mathrm{amtofenzymebeforeimmobilization}} * 100$$

Eq. (B.1)

The binding capacity of Rif@UiO-66 was assessed by incubating 10 mg of the specimen with ascending levels of LysB-D29 (in 50 mM Tris-HCl buffer, pH 7.4) at 4°C overnight with continual shaking. Subsequently, Rif@UiO-66 was washed, and the amount of immobilized enzyme was determined as described in [28].

To estimate the binding capacity, the following equation was used:

$\mathrm{Bindingcapacity}$ (mg enzyme/mg Rif@UiO-66)

$$= \frac{\mathrm{amtofimmobilizedenzyme}\,(\mathrm{mg})}{\mathrm{wtofRif@UiO} - 66\ (\mathrm{mg})}$$

Eq. (B.2)

2.8. Enzymatic Activity of Free and Immobilized LysB-D29 assays

The esterase activity of the purified LysB enzyme was measured for the formation of para-nitrophenol at 410 nm, resulting from the hydrolysis of p-nitrophenyl palmitate (p-NPP). Twenty microliters of buffer and Rif@UiO-66 were used as controls for free and immobilized enzymes, respectively. The reaction rate was calculated from the slope of the linear part of the kinetic curve [21, 22, and 28]

To measure the specific enzymatic activity and enzymatic activity for free lysB, the following equations were used: [**equations SB1, SB2**]

The specific enzymatic activity of the immobilized enzyme was calculated using the following equation:

$$\mathrm{Units/mgimmobilizedenzyme} = \frac{Activity\left(\frac{U}{ml}\right)}{\mathrm{LysB/Rif@UiO} - 66\mathrm{concentration(mg/ml}}$$

Eq. (C.1)

The enzymatic activity of the immobilized enzyme was calculated as follows:

$$\text{Activity } (\frac{U}{ml}\text{ immobilized enzyme} = \frac{(\Delta A410\text{ test} - \Delta A410\text{ blank}) \times (\text{total volume})}{\varepsilon \times (\text{Volume of immobilized enzyme })}$$

Eq. (C.2)

Where:

One unit (U) of enzyme activity corresponds to the amount of enzyme releasing 1 µmol of p-nitrophenol/min through the test conditions; ε is the extinction coefficient of p-nitrophenol

2.9. Rifampicin and LysinB enzyme release and kinetic studies

To obtain the release pattern of Rif and lysB enzyme release behavior from synthesized UiO-66, 5.0 mg of Rif@UiO-66 was incubated in 50 mL of 0.1 M phosphate buffer saline (PBS), pH 7[26]. The solution was placed in a dialysis bag (MWCO 12,000–14,000 Da, Himedia, India) under sink conditions at 37°C. These conditions were obtained to resemble the physiological conditions of the body and intracellular environment of infected macrophages, respectively. Then, samples were withdrawn at predetermined time intervals [26]. Then, 1 mL of dialysate was replaced by 1 mL of fresh PBS. The sample release was based on its concentration at a certain time and actual drug and enzyme content in UiO-66. The release experiments were carried out three times, and the average values were reported. The kinetic data of Rif and lysB were analyzed by the zero-order, Higuchi, and Korsmeyer-Peppas pharmacokinetic models to obtain the drug release mechanism from UiO-66[29].

2.10. Determination of minimum inhibitory concentration (MIC) and minimum bactericidal concentration (MBC)

MIC was assessed by the broth macrodilution procedure. One hundred microliters of various levels of the rifampicin, UiO-66 metal organic frameworks Rif@UiO-66 and lysB/Rif@uio-66 nanocomposites (5000 to 10000, 20 µg/mL) were added to the broth. Twenty-five microliters of a fresh test microorganism was added to 2 mL of the nutrient broth to obtain the starting inoculums. MBC determination was carried out by plating the suspension from each tube into an MHA plate. The plates were incubated at 37°C for 24 h [30].

2.11. Microscopic examination of bacterial cells

M. smegmatis cells were obtained using centrifugation at 5000 × g for 15 min at 4°C from a 24-hour culture in nutrient broth. The samples were fixed in 3% glutaraldehyde, rinsed in phosphate buffer, postfixed in potassium permanganate solution for 5 min at ambient temperature, dehydrated, and then penetrated with epoxy resin and acetone after being washed with distilled water. On copper grids, very thin pieces were gathered. After that, the sections were stained three times with lead citrate and uranyl acetate. A JEOL - JEM 1010 TEM operating at 80 kV was used to view stained sections at the Regional Centre for Mycology and Biotechnology (RCMB), Al- Azhar University. [31]

2.11. In vitro cell cytotoxicity assays

To perform the MTT assay for toxicity evaluation, mammalian cells from African green monkey lung (Vero) were exposed to an aqueous solution containing rifampicin, Rif@uio-66 and lysB/Rif@UiO-66 nanocomposites for 48 h at 37°C. After dissolving the MTT precipitate, the absorbance was measured at 590 nm [32].

2.12. In vivo studies

2.12.1 Animals and ethics

Male Wistar albino rats were bought from the Nahda University animal house in Beni-Suef, Egypt, and kept in polypropylene cages (five animals per cage) for the duration of the experiment under normal conditions of temperature (25 ± 5°C), relative humidity (55 ± 5%), and 12-hour light/dark cycles. Ad libitum access to filtered water and a standard pellet diet were made available under hygienic settings. Prior to the tests, the rats had a one-week acclimatization period. Animal studies were approved by the Institutional Animal Care and Use Committee (IACUC) of Beni-Suef University (IACUC Permit Number: BSU-FS-2022-12).

2.12.2. Experimental design

Male Wistar albino rats (200–250 g, 11–12 weeks) were divided in a random way into 6 groups (5 rats/each group): blank group I (received no drug), animals were intratracheally injected using 1X106 M. smegmatis to induce pulmonary infection for the rest of the groups, where the rest of the groups revived various treatments for 24 and 48 hr.

The second positive control group, group II, received LPS, group (3) was administered rifampicin [33], group (4) was treated with 1 mg/kg UiO-66 [33], group (5) was treated with Rif@UiO-66, and group (6) was treated with lysB/Rif@UiO-66.

After intra-abdominal anesthetization using 20% urethane solution (v/v, 5 mL/kg), the rats were intratracheally administered Rif, Rif@UiO-66 and LysB/Rif@UiO-66 (equivalent to a dose of 50 mg/kg of Rif) and 1 mg/kg of Uio-66 according to [33] by a DP-4 dried powder insufflator (PennCentury Inc., China) or LPS solution (3 mg/kg) by an endotracheal dispersion device (HRH-MAG4, HM). An endotracheal tube was placed into the open rat trachea at 24 and 48 hours after dosing. After that, 1 mL of PBS was pumped into the lungs via a tube, and bronchoalveolar lavage was performed three times. Centrifuging of the bronchoalveolar lavage fluid (BALF) took place at a speed of 700 × g for 15 minutes at 4°C. For further investigation, the supernatant was obtained and kept at -80°C. The concentrations of inflammatory mediators (IL-1, IL-6, MIP-1, and TNF-) in BALF were assessed using a specialized test kit.

Lactate dehydrogenase (LDH) was measured using an LDH assay kit, and total protein was determined using a BCA measuring proteins kit [34].

2.12.3. Histopathological analysis of rat lung and liver

Slices of 5 mm thick liver and lung tissues were made, fixed in 10% neutral buffered formalin (10% NBF), dehydrated in ethanol at various concentrations, washed in xylene, and then embedded in paraffin. The paraffin blocks were sliced with a microtome at a thickness of 4–6 m and stained with hematoxylin and eosin to examine the general tissue structure. Sections stained with hematoxylin and eosin were examined using a Leica microscope (CH9435 Hee56rbrugg) (Leica Microsystems, Switzerland) in accordance with the instructions provided by [35].

2.12.4. In vivo biodistribution studies

The concentrations of rifampicin in various processed organs were detected by high-performance liquid chromatography (HPLC) as reported previously with some changes [36, 37].

The rats were given a repeated dose of 50 mg/kg intratracheal administration (equivalent to a dose of 50 mg/kg of Rif in each group). The rats were split into three groups: Group I rats received Rif (50 mg/kg), and Group II rats received Rif@UiO-66 (equivalent to a dose of 50 mg/kg of Rif). Rats treated with LysB/Rif@UiO-66 (equivalent to a dose of 50 mg/kg of Rif) (Group III). At 24, 48 and 72 hrs. The animals were sacrificed. The organs (lung, liver, spleen, heart, brain, and kidney) were removed, immediately rinsed with normal saline to eliminate any visible blood, packed in aluminum foil and kept at -20°C in sterile containers. Drug levels were assessed in 20% (w/v) tissue homogenates made in normal saline using the exact weights of the thawed tissues. Protein precipitation was used to prepare the samples, which were subsequently centrifuged at 21,000 × g for 10 min at 4°C. To determine the concentration of Rif in each tissue, the supernatants were removed, filtered through a 0.2 m syringe filter, and then injected onto the HPLC column. In terms of tissue, the data are given as mg/kg. Rats were slaughtered at 24 h, 48 h, and 72 h for all samples to examine the impact of various Rif formulations on rat organs.

2.13. Docking:

Molecular docking, a well-known and adaptable in silico technique, makes it possible to choose biologically advantageous templates from libraries of compounds before they are created. It predicts how the best conformers of different ligands would interact with the receptor protein, helping to specify the synthetic targets. Using the Molecular Orbital Environment (MOE) program, we developed complete molecular docking analyses of rifampicin and Uio-66 to investigate the binding modes between the ligands and the intended enzyme, lysin B from Mycobacteriophage D29 (3HC7). ChemDraw Ultra 12.02 was used to draw the structures of each chemical, and these structures were saved as MDL files (".sdf") for MOE to display.

The protein data bank [38] provided the crystal structures of lysin B from Mycobacteriophage D29 (3HC7). After the water molecules surrounding the protein were eliminated, hydrogen atoms were added. The MMFF94x force field was used to assign the parameters and charges. Our compounds were docked in the active site using the DOCK module of MOE after alpha-site spheres were created using the site finder module of MOE. The London dG scoring formula, placement: triangle matcher, retain 10, and refinement: Force fields were used to determine the dock scoring for the MOE program. By taking into account the RMSD values, binding energies, and binding modes with the selected residues, the leading conformations of the docked ligands were established.

2.13. Statistical analysis

Three independent replicates were used for each experiment. Dunnett's multiple comparisons test, a component of a two-way ANOVA, was used to evaluate whether there were significant differences between the data sets. Data are expressed as the mean of the triplicates ± standard deviation (SD). Statistics were deemed significant at $^{**}p < 0.01$ and $^{****}p < 0.0001$.

3. Results and Discussion

3.1. Characterization

3.1.1. XRD

Powder XRD was conducted to investigate the structural properties of the obtained UiO-66, the standard rifampicin and the Rif@UiO-66 nanocomposite. Figure 1**A** shows the XRD patterns of the samples. For the as-prepared UiO-66, there are three main characteristic peaks at $2\theta = 7.4°$, 8.5° and 25.8°, which are assigned to the (111), (002) and (006) planes of UiO-66, respectively, and are in great accordance with results reported earlier[39]. In addition, a weak peak at 12.0° can probably be attributed to the presence of the diagonal linkers combined with the strong interaction of linker − inorganic brick in the metal organic framework of UiO-66 [40].

After loading of Rif on the metal organic framework, the position of the characteristic Bragg peaks for the UiO-66 nanocomposite shows no shift, indicating no alteration in the crystalline structure of the UiO-66 nanocomposite. However, compared with the patterns of UiO-66 before loading, a significant decrease in the peak relative intensity was observed for Rif@UiO-66, which could be ascribed to the trapping of Rif in the UiO-66 pores and consequently results in decreased X-ray contrast between porous metal organic frameworks and pore cages [41].

3.1.2. FTIR

The FTIR spectra of UiO-66 shown in **Fig. 1B** and **Table S1** are notably similar to those reported in previous studies in the open literature [42–45]. The spectrum can be divided into five zones. The first zone consists of various bands that are assigned to the vibrations of (−O-H), such as the observed broad peaks at 3751, 3411.517 and 3414.801 cm^{-1} [44].

The second zone at 1664, 1587, 1510 and 1403 cm$^{−1}$ is related to the carboxylate ligands. More precisely, strong bands at 1587 and 1410 cm$^{−1}$ were observed, which belong to the O-C-O asymmetric and symmetric stretching in the BDC ligand [42, 43]. The bands appearing at 1631.568 and 1435.625 cm$^{−1}$ in the drug spectrum are attributed to the characteristic furanone C = O and amide CO frequencies. The spectra also show sharp and strong bands at 1422.165 and 1435.067 cm$^{−1}$ due to (C = N) related to Rif@UiO-66 and the drug. [46]. The third zone at 1153, 1095 and 1010 cm-1 belongs to C = N amino groups on the benzene ring, and the phenolic (C-O) spectra appeared at 1049.318, 1090.662, and 1101.867 cm$^{−1}$ for Rif@ UiO-66, UiO-66, and standard Rif, respectively [26, 44, 45]. The fourth zone at 808, 743, and 662 cm$^{−1}$ is combined with C-H vibration, C = C stretch, OH bend and O-C-O bend in the BDC ligand [44]. The end zones at 662, 550 and 482 cm$^{−1}$ belong to μ3-O vibration bending, Zr(O-C) stretches and μ3-OH asymmetric stretching, respectively. The FTIR spectrum of Rif@UiO-66 represents the Rif-entrapped molecules in UiO-66. The disappearance of the amide (C = O) band in the spectrum of Rif@UiO-66 elucidated the deprotonation of the phenol group to coordinate with the drug. Additionally, shifting of the (C = O) frequency in the drug and UiO-66 from 1664.117 and 1631.568 cm$^{−1}$, respectively, to 1571.843 cm$^{−1}$ in the nanocomposite illustrates the coordination.

3.1.3. Thermogravimetric analysis

As shown in **Fig. 1C and Fig. 1S**, thermogravimetric analysis (TGA) was carried out to evaluate the thermal stability of UiO-66 and Rif@UiO-66. TGA curves of the two samples showed that the thermal degradation of the samples passes through three progressive weight-loss steps. First, for UiO-66, the initial weight-loss step starts at room temperature and ends at approximately 150°C. This weight loss might be due to the desorption of physiosorbed water and evaporation of other volatile materials [47]. The second step starts gradually until 300°C, and then the degradation becomes rapid until 500°C. This step represents the main degradation of UiO-66, which is related to the removal of the (DMF) solvent and monocarboxylate ligands and the dehydroxylation of the zirconium cornerstones [48, 49]. The third weight–loss step starts at 500°C, which is attributed to the decomposition of inorganic fragments such as benzene fragments; in other words, this is a result of the burning of organic-linker molecules in UiO-66, but in this stage, ZrO_2 remains[47]. For Rif@UiO-66, TGA showed the same three steps as UiO-66, while a change in weight loss occurred upon heating Rif@UiO-66 to 600°C. The first weight-loss step starts slowly until 250°C. The second step weight loss starts rapidly until 375°C and continues degradation in the third step until 600°C. Rif@UiO-66 began to decompose at approximately 250°C, which means that added functional groups led to a reduction in the thermal stability of UiO-66. However, they still had high thermal stability, which was suitable for drug delivery at body temperature [49].

3.1.4. Surface porosity and surface area

The Brunauer–Emmett–Teller (BET) theory was employed for estimating the surface porosity, the surface area, the cavities of MOFs, and the drug molecules trapped within its pores [50]. As illustrated in the BET plots in **Fig. 1D**, N_2 adsorption – desorption isotherms were utilized to investigate the textural properties of UiO-66, Rif@UiO-66 and LysB/Rif@UiO-66. The isotherm for all samples was determined as a type IV sorption isotherm according to the IUPAC Classification of Isotherms, which is characteristic of microporous materials [51]. This means that the amount of N_2 adsorption decreased by the loading of Rif and by immobilization of the lysB enzyme. A decrease in peak strength provides evidence supporting that most pores of UiO-66 may be blocked during drug loading and enzyme immobilization within the network of UiO-66 [52]. As shown in **Table 1 and Fig. 1**S, the specific surface areas of the sample UiO-66 before and after loading of Rif are 834 m^2/g and 651 m^2/g, respectively, and 374 m^2/g after enzyme immobilization of LysB/Rif@UiO-66. There was a decrease in the total pore volume from 1.040 cc/g in the case of UiO-66 to 0.866 cc/g for Rif@UiO-66 and 0.2594 cc/g for LysB/Rif@UiO-66. These results strongly indicate that the drug and enzyme were approximately loaded and immobilized onto Uio-66. The Barrett, Joyner and Halenda (BJH) theory was used to estimate the actual pore size in the characterization of porous materials [53]. The pore size was determined to be smaller than 20 Å for UiO-66, and the mean pore widths were 19.28, 19.02 and 19 Å.

Table 1
Specific surface area **(m^2/g)**, and pore size **(Å)**, total pore volume **(cc/g)** for UiO-66, Rif@UiO-66, and LysB/Rif@UiO-66.

Sample	**Surface area (m^2/g)**	**Pore size (Å)**	**Total pore volume (cc/g)**
UiO-66	834	19.2	1.040
Rif@UiO-66	651	19.02	0.866
LysB/Rif@UiO-66	374	19	0.2594

3.1.5. Surface charge and DLS analysis

Figure 2 shows the results of surface charge analysis and the hydrodynamic particle size of the synthesized UiO-66, Rif@UiO-66 and LysB/Rif@UiO-66 [54]. The surface charge of the Rif and LysB enzyme in the same solution with the same pH was close to zero. The immobilization of enzymes on Rif@UiO-66 showed the same results as those observed for Rif@UiO-66, as shown in Table 4. These results indicate that the suspension of the particles in a medium increases by increasing the negative surface charge easing the negative surface charge, which is attributed to the repulsive forces among the particles. In our study, the prepared samples had a high negative charge, which means that a stern layer of positively charged ions (counter ions) from the solution was unrelentingly attached to the colloid. As shown in **Table 2**, the surface charge of Rif is close to zero. [55, 56]

The hydrodynamic particle sizes of Rif@UiO-66 and LysB/Rif@UiO-66 were 129 and 131 nm, respectively, which were slightly larger than that of UiO-66 at 90 nm. The polydispersity indices (PDIs) were 0.281 ± 0.01, 0.312 ± 0.02, and 0.362 ± 0.01 for UiO-66, Rif@UiO-66 and LysB/Rif@UiO-66, respectively.

Table 2

DLS, PDI and zeta potential of UiO-66, rifampicin, LysB enzyme Rif@UiO-66, LysB/Rif@UiO-66, and rifampicin

Samples	Z-average size (nm)	PDI	Zeta Potentials (mv)
UiO-66	90 ± 10	0.281 ± 0.010	-30.1 ± 2
Rif@UiO-66	129 ± 12	0.312 ± 0.11	− 32.12 ± 1
LysB/Rif@UiO-66	129 ± 8	0.362 ± 0.01	-31.1 ± 3
Rifampicin	_	_	0.003 ± 0.01
LysB enzyme	_	_	0.021 ± 0.01

3.1.6. Morphology study

Figure 3 presents the HRTEM images performed to further demonstrate that all the synthesized MOFs have good structures. UiO-66 had a particle size of approximately 25 nm, with a uniform rhombic dodecahedral shape **(Fig. 3A).** The Rif@UiO-66 morphology and particle size were significantly unchanged, showing a particle size of 26 nm **(Fig. 3C)**. Figure 3**B** represents the particle size distribution of UiO-66, showing an average particle size of 25.8 ± 0.51 nm. The particle size distribution of Rif@UiO-66 showed an average particle size of 26.8 ± 2.07 nm (**Fig. 3D**). This indicates that the size of UiO-66 was unaffected by drug loading.

As demonstrated by the SEM image, the morphology of UiO-66 resembles an unchanging rhombic dodecahedron aggregate with a particle size distribution of 20.77 ± 3 (**Fig. 3E, 3F**). The SEM images of Rif@UiO-66 outline the adjustment in edge thickness compared with UiO-66 with a particle size distribution of 26.70 ± 0.5 (**Fig. 3G, 3H**). No clear accumulation or damage in crystal structure was observed by SEM, which indicates that Rif molecules are inserted into the pores inside or to the outside surface of the synthesized UiO-66 system.

3.2. Loading capacity and encapsulation efficiency

The drug loading rate for Rif@UiO-66 microspheres was 12.1 ± 0.12% w/w, with an encapsulation efficiency of 80.72 ± 2.23%. This result is similar to that found in the literature [27].

3.3. Immobilization yield% and enzymatic activity of free LysB and LysB/Rif@UiO-66 nanocomposite

Table 3. After the confirmation of the Rif@UiO-66 structure, the LysB enzyme was immobilized onto the Rif@UiO-66 nanocomposite by physical adsorption. The immobilization yield was 81%, and the quantitative yield of immobilized LysB was 60 mg/g. The enzyme activity of LysB/Rif@UiO-66 (2.91 U/mg) was slightly higher than that of free LysB, which was approximately 2.59 U/mg. LysB/Rif@UiO-66,

showing a higher specific activity compared to that of free LysB. The specific activity of LysB/Rif@UiO-66 was 0.78 U/mg higher than that of free LysB, which was 0.56 U/mg. This improvement may be due to the larger and more ordered pores of UiO-66.

Table 3

Immobilization of LysB by Physical Adsorption to Rif@UiO-66 nanoparticles at pH 7.4. The results in this table are expressed as the mean ± SD (n = 3). LysB (1.5 mg) was mixed with 20 mg Rif@UiO-66.

Sample	**Immobilization yield (%)**	**Amt protein immobilized (mg/g Rif@ UiO-66)**	**Total protein immobilized (mg)**	**Activity (U/mg)**	**Specific activity U/mg)**
Free LysB				2,59 ± 0.12	0.56 ± 0.02
LysB/Rif@UiO-66	81% ±1.5%	60 ± 1	1.21 ± 0.10	2.91 ± 0.09	0.78 ± 0.03

3.4. In vitro drug and enzyme release study

The in vitro release study revealed that Rif-loaded UiO-66 could provide a longer and more sustained release compared with pure drug **(Fig. 4A).** Rif release from Rif@UiO-66 can be divided into two stages: a quick phase during the initial 8 h, where approximately 58% of the drug was released, and a slow phase during the subsequent 40 h. Rif release from Rif@UiO-66 reached a plateau after 12 h, and the released amount at this point was equivalent to 71% of the loaded amount of Rif that showed sustained release of the drug. Figure 4B shows the in vitro release of the LysB enzyme from lysB/Rif@UiO-66. One hundred percent of the nonimmobilized enzyme was released in the first 2 hours, but the immobilized enzyme was released completely after 4 hours.

Regarding the release kinetic models for Rif and LysB (**Table 2S**), one can notice that incorporating Rif into UiO-66 MOF notably changed the release kinetics from the Hixson model, which is primarily dependent on dissolution speed, to zero-order release, which is independent of dissolution and diffusion speeds, with a sustained release pattern. Incorporating LysB into UiO-66 MOF did not result in a change in release patterns, which was consistent with the Higuchi diffusion model [29].

3.5. Anti-mycobacterial activity

To evaluate the antimycobacterial activities of the materials, the MICs and MBCs of the Rif, UiO-66, LysB enzyme, and Rif@UiO-66 and LysB/Rif@UiO-66 nanocomposite were determined against M. smegmatis as a model microorganism. **Table 5** shows the results of the MICs and MBCs of different samples. The MIC of LysB/Rif@uio-66 was 9.7 µg/mL, which was 16-fold lower than that of pure Rif, which was 156.25 µg/mL. The MIC of Rif@UiO-66 (39 µg/mL) was 4-fold lower than that of pure Rif. The MBCs of LysB/Rif@UiO-66 (19.5 µg/mL) and Rif@UiO-66 (78.1 µg/mL) were 16- and 4-fold that of pure Rif, which was 312.5. The MICs of UiO-66, LysB and the synergistic effect between Rif and LysB were > 2500, 1250 and 78.125 µg/mL, respectively. These results indicate that UiO-66 and LysB have slight antimicrobial activity. As shown in **Table 3S**, the MIC and MBC of this nanocomposite were 8-10-fold higher than those found in the literature [57–62]. The improvement and a significant decrease in MIC were attributed to the LysB/Rif@UiO-66 nanocomposite's unique properties, allowing penetration of the cell wall or rupture. UiO-66 MOFs act as a delivery vehicle that facilitates the easy entry of antibiotics with the help of the LysB enzyme into target cells. In other words, this nanocomposite may have an important role in minimizing the need for a high dose of antibiotic, which is required due to loss blood circulation. Several investigators reported the successive impact of nanocomposites as potent anti-biofilms due to their efficient properties to target essential bacterial structures [63, 64].

Table 4
Antimycobacterial activity of the different samples compared to standard rifampicin evaluated as MIC and MBC against M. smegmatis. The results in this table are the average of triplicates.

Samples	MIC (µg/mL)	MBC (µg/mL)
Rifampicin	156.25	312.5
Rif@Uio-66	39.0	78.125
LysB/Rif@Uio-66	9.7	19.5
UiO-66 MOFs	>2500	> 2500
LysB	1250	> 2500
Rifampicin with LysB	78.125	156.25

3.6. TEM for M. smegmatis

Figure 5 shows TEM micrographs of the negative control and treated cells of M. smegmatis. The cells of the control show a clear, intact cell wall and cell membrane enclosing the cytoplasm. The cell morphology was maintained, showing the well-known rod-shaped form **(Fig. 5A).** Upon treatment with LysB/Rif@UiO-66 and Rif, the cells lysed with obvious release of the intracellular content and formation of intracytoplasmic lipid inclusions. Ultrathin sections of M. smegmatis that had been exposed to Rif and LysB/Rif@UiO-66 revealed that cellular damage and intracellular material leakage eventually with the formation of intracytoplasmic lipid inclusions (ILI) resulted in total cell deformation, with amazing destruction of cells affected, leading to complete cell death **(Fig. 5B and 5C).** The antibacterial effect of the MOF/phage-antibiotic combination is mediated by suppression or control of the enzymes responsible for cell wall construction, nucleic acid metabolic processes, maintenance, the production of proteins, and rupture of the membrane structure. In general, physical harm to bacterial cells is a component of the antibacterial effect of MOFs [65]. The prepared MOF/phage-antibiotic combination may have caused damage to the cell wall. [66–68].

3.7. In vitro cytotoxicity

The biocompatibility of nanomaterials is a major concern in practice. In vitro cytocompatibility studies are the standard tests for determining the biocompatibility of a biomaterial. The results exhibited in **Fig. 5D** show that Rif@UiO-66 and LysB/Rif@UiO-66 had favorable biocompatibility, and the cell viability value was 97% at a rifampicin concentration of 7.8 μg/mL. Rif@UiO-66 and LysB/Rif@UiO-66 had slight differences in cell viability, which was 100% at concentrations ranging from 0 to 62.5 μg/mL.

Previous studies reported that UiO-66 nanocarriers were nontoxic at low concentrations, which was consistent with our results. This highlights the potential of UiO-66 as a promising candidate for pulmonary drug delivery [34].

3.8 In vivo study

3.8.1. In vivo toxicity and inflammatory effects

The quantities of inflammatory cytokines (IL-1, IL-6, MIP-1, and TNF-) in BALF were assessed to examine inhalation toxicity and inflammatory effects **(Fig. 6)**. If the sample irritates the respiratory system and lungs, the body will respond by becoming more inflammatory, and the expression of inflammatory cytokines will increase. LPS was administered as a positive control since it has the potential to cause inflammation [69]. The levels of inflammatory mediators in the BALF of rats treated with various specimens after 24 h are depicted in **Fig. 6B**. The levels of IL-1β, IL-6, MIP-1α, and TNF-α in the LPS group were much higher than those in the blank group, UiO-66 group, Rif group, Rif@UiO-66 group, and LysB/Rif@UiO-66 group, revealing that inflammation was induced by LPS. There was no significant difference in the concentrations of inflammatory mediators among the blank group, UiO-66 group, Rif group, Rif@UiO-66 group, and LysB/Rif@UiO-66 group. These results showed that UiO-66 and rifampicin did not enhance the inflammatory response. The concentrations of inflammatory mediators in BALF after 48 h were further measured. The concentrations of IL-1β, IL-6, MIP-1α, and TNF-α in the LPS group were higher than those in the other groups. It should be noted that the levels of inflammatory mediators at 48 h for the Rif group were slightly higher than those for the blank group, UiO-66 group, Rif@UiO-66 group and LysB/Rif@UiO-66 group, indicating that Rif might cause mild irritation. The protein levels and LDH in BALF at 48 h were also measured **(Fig. 2S and 3S).** The protein levels and LDH of the LPS group were higher than those of the other groups, which was consistent with the results of inflammatory mediators demonstrating the excellent biocompatibility of UiO-66, Rif@UiO-66 and LysB/Rif@UiO-66 nanocomposites.

3.8.2 Histopathology of liver and lung tissues

3.8.2.1. Liver tissue

The effects of Rif, UiO-66, Rif@uio-66 and LysB/Rif@UiO-66 on the liver and lung tissues were investigated. The image of liver tissue sections of rats in the negative control group was normal (**Fig. 7A)**. The figure shows the portal area with normal constituents of the portal vein, hepatic artery, and bile duct (cube). Hepatocytes had a regular cord appearance with polygonal cells with spherical and central nuclei (thick arrow).

On the other hand, rats that received free Rif had several degenerative changes in the liver cells with a clear loss of cellular regularity. The portal area shows a congested portal vein (arrowhead) with considerable infiltration of inflammatory cells accompanied by edema (thin arrow). Several vacuolated and apoptotic hepatocytes were observed (thick arrow) with interstitial hemorrhage between hepatic cords (circle) (**Fig. 7B**). The hepatotoxicity of rifampicin was detected earlier in [70]. Rats treated with Uio-66 showed better liver structure; however, the portal area still showed a congested portal vein (arrowhead) with infiltrated inflammatory cells (cube). Hepatocytes were in normal vesicular form (thick arrow), with some cells displaying vacuolated apoptotic morphology (thin arrow) with normal assembly of hepatic sinusoids (circle) (**Fig. 7C**). Liver sections of the Rif@UiO-66-treated group showed moderate enhancement with a congested portal vein (arrowhead) and accumulation of inflammatory cells (cube). Hepatocytes showed both normal vesicular (thick arrow) and apoptotic forms (thin arrow) (**Fig. 7D**). As shown in **Fig. 7E**, LysB/Rif@UiO-66 displayed the best progress in liver tissue with scarce inflammatory cells (cube). Hepatocytes (thick arrow) and hepatic sinusoids (circle) were displayed in their normal assembly, similar to the negative control group.

3.8.2.2. Lung tissue

(Fig. 7.) demonstrates the effects of the different preparations on lung tissues where they initially exhibit normal structures of bronchiole (cube) and alveoli (thick arrow) in the negative control group **(Fig. A).** Lung sections of the Rif group showed serious deteriorating variations, seen as loss of alveoli normal regularity with obvious thickening of their membrane (cube). This was accompanied by edema leading to dispersion between alveoli (thin arrow), in addition to aggregation of white fat cells (arrowhead) (**Fig. 7B**). For the group treated with UiO-66 nanoparticles, a moderately advanced lung structure was observed with a noticeable decrease in alveolar wall thickness. The blood vessels were congested (circle) with some aggregated inflammatory (cube) and fat cells (arrowhead) (**Fig. 7C**). Rif@UiO-66 nanoparticles revealed moderate enhancement with the exception of interstitial edema (thin arrow) with aggregated inflammatory cells (cube) and white fat cells (arrowhead) **(Fig. 7D)**. As shown in **Fig. 7E**, the best progress was observed along the alveolar structure (arrow). Notice little congestion (circle) as well as little inflammatory cell infiltration (cube). Treatment with the LysB/Rif@UiO-66 nanocomposite had the best curative impact versus pulmonary histological examination of the lung.

3.8.3 In vivo biodistribution studies

After inhaling free Rif solution, Rif@UiO-66, and LysB/Rif@UiO-66, the biodistribution profile of Rif in various organs was assessed in rats at three distinct time points (24 h, 48 h, and 72 h) [71]. According to in vivo biodistribution investigations, pure Rif solution was most abundantly deposited in the liver, lung, and kidneys after 24 and 48 hours **(Fig. 8B).** Singh et al. published on the use of rifampicin lipospheres in lung infections (Singh et al., [71]). This suggests that the organ distribution profile of Rif is quick and general. Additionally, by the 72-hour mark, no drug was found in any of the organs, indicating that the pure drug had completely left the body.

Lung > Spleen > Kidney > Liver > Heart > Brain has been shown to be the sequence of drug deposition for Rif@UiO-66 at 24 hours in diverse organs. The biodistribution profile at 48 and 72 hours also showed the same progression: Lung > Liver > Kidney > Spleen > Brain > Heart.

At 24, 48, and 72 hours, Rif@UiO-66 showed the greatest drug concentration in the lungs. Furthermore, after 24 and 48 hours, Rif@UiO-66 demonstrated substantially 1.7- and 4.63-fold greater lung uptake than pure Rif solution, respectively. Histopathological analysis of liver tissue revealed that the free Rif concentration in the liver was much greater than that of its NPs within the first 24 and 48 hours, suggesting the likelihood of hepatotoxicity. The order of LysB/Rif@UiO-66 medication concentration at 24 h in different organs was discovered to be lung > kidney > spleen > liver > brain > heart. The sequence of the biodistribution profile at 48 and 72 hours is identical to the order of the concurrent Rif@UiO-66.

The amount of the drug found in the lungs after 24 hours in the case of LysB/Rif@UiO-66 was comparable to that of Rif@UiO-66. When compared to Rif@UiO-66 (1.14-fold) and free Rif solution (5.31-fold), LysB/Rif@UiO-66 showed a greater concentration in the lungs after 48 hours. The use of UiO-66 as a carrier, which is stable in the neutral pH aqueous environments found in the body, may be the cause of the increased lung uptake of lysB/Rif@UiO-66. As a result, any potential complications from long-term accumulation would be avoided [73]. Additionally, because of the negative charge of the Rif@UiO-66 and LysB/Rif@UiO-66 nanocomposites (measured to be -31 mV), they are internalized mainly by phagocytic cells and persist in the lung [74].

4. Molecular modeling: docking study

As shown in **Fig. 8C, D, and E and Tables 4S and 5S**, rifampicin and UiO-66 were subjected to molecular docking experiments against lysin B from mycobacteriophage D29 (3HC7) as further support for biological screening investigations. The results, which are compiled in Tables 4S and 5S, showed that the docking and experimental results had a very high degree of agreement. We found that the ligands for rifampicin and uio-66 were − 6.93606 and − 6.7957 Kcal/mol, respectively. The H-acceptor relationship between O 109 of rifampicin and the TYR 168 residue of the 3HC7 enzyme was discovered, as was the interaction between O 15 of UiO-66 and the MET 167 residue, according to the two-dimensional maps of these ligands. As evidenced by its positive contacts with the selected residues, strong RMSD values, and good docking score, rifampicin and UiO-66 exhibited the most effective in silico inhibition of the 3HC7 enzyme.

5. Conclusion

Thus, it can be concluded that a novel innovative combination of LysB/Rif@UiO-66 may be used successfully in the management of tuberculosis by enhancing the effectiveness of the conventional rifampicin regimen to treat it by streamlining dosing, minimizing side effects, and improving enzyme-antibiotic therapy. Intriguingly, this nanocomposite improves bioavailability in the lungs and reduces hepatotoxicity linked to anti-tuberculosis medications requiring inhalation delivery, increasing the chance of eliminating existing drug resistance mechanisms instead of utilizing the drug alone. The combination of enzyme therapy and nanotechnology opens up new avenues in tuberculosis treatment and addresses the urgent need for alternative strategies against drug-resistant strains. Our findings might provide insight into the Mofs-release vehicle for enzyme-antibiotic antitubercular therapy.

Declarations

Credit authorship contribution statement

Zienab E. Eldin: Formal analysis, investigation, methodology, validation, visualization, data curation, funding acquisition, formal analysis, roles/writing - original draft; writing - review & editing. **Tarek Dishisha:** Supervision. **Ahmed Farghali:** Supervision**.** ***Hanaa.M.* Salama:** Software. **Ossama M. Sayed**: Supervision.

Declaration of Competing Interest

The authors declare that they have no known competing financial interests or personal relationships that could have appeared to influence the work reported in this paper.

Acknowledgments

The authors are thankful to all members of the Materials Science and Nanotechnology Dept., Faculty of Postgraduate Studies for Advanced Sciences (PSAS), Beni-Suef University Egypt, for supporting the preparation of the nanomaterials. All members at Central Lab for Characterization.

Funding

This research did not receive any specific grant from funding agencies in the public, commercial, or not-for-profit sectors.

Consent for publication

The authors approved this version of the manuscript for publication.

Data availability

Data will be made available on request.

References

1. Pai M, Behr MA, Dowdy D, Dheda K, Divangahi M, Boehme CC, Ginsberg A, Swaminathan S, Spigelman M, Getahun H, et al: **Tuberculosis.** *Nature Reviews Disease Primers* 2016, **2:**16076.
2. Organization WH: **Global Tuberculosis Report 2021.** *Reports* 2021.
3. Bourzac K: **Infectious disease: beating the big three.** *Nature* 2014, **507:**S4-S7.
4. Rahlwes KC, Dias BR, Campos PC, Alvarez-Arguedas S, Shiloh MU: **Pathogenicity and virulence of Mycobacterium tuberculosis.** *Virulence* 2023, **14:**2150449.
5. Ranjitha J, Rajan A, Shankar V: **Features of the biochemistry of Mycobacterium smegmatis, as a possible model for Mycobacterium tuberculosis.** *Journal of infection and public health* 2020, **13:**1255-1264.
6. Lelovic N, Mitachi K, Yang J, Lemieux MR, Ji Y, Kurosu M: **Application of Mycobacterium smegmatis as a surrogate to evaluate drug leads against Mycobacterium tuberculosis.** *The Journal of antibiotics* 2020, **73:**780-789.
7. Suárez I, Fünger SM, Kröger S, Rademacher J, Fätkenheuer G, Rybniker J: **The diagnosis and treatment of tuberculosis.** *Deutsches Aerzteblatt International* 2019, **116**.
8. Bi K, Cao D, Ding C, Lu S, Lu H, Zhang G, Zhang W, Li L, Xu K, Li L: **The past, present and future of tuberculosis treatment.** *Journal of Zhejiang University (Medical Science)* 2023, **51:**657-668.
9. Rossi ED, Aínsa JA, Riccardi G: **Role of mycobacterial efflux transporters in drug resistance: an unresolved question.** *FEMS microbiology reviews* 2006, **30:**36-52.
10. Hakkimane SS, Shenoy VP, Gaonkar SL, Bairy I, Guru BR: **Antimycobacterial susceptibility evaluation of rifampicin and isoniazid benz-hydrazone in biodegradable polymeric nanoparticles against Mycobacterium tuberculosis H37Rv strain.** *International journal of nanomedicine* 2018**:**4303-4318.
11. Reuter A, Apolisi I, Daniels J, Furin J, Cox H: **Household contact management for rifampicin-resistant tuberculosis.** *The Lancet Global Health* 2022, **10:**e1387.
12. Toft AL, Dahl VN, Sifna A, Ige OM, Schwoebel V, Souleymane MB, Piubello A, Wejse C: **Treatment outcomes for multidrug-and rifampicin-resistant tuberculosis in Central and West Africa: a systematic review and meta-analysis.** *International Journal of Infectious Diseases* 2022, **124:**S107-S116.
13. Kim M, Jo Y, Hwang YJ, Hong HW, Hong SS, Park K, Myung H: **Phage-antibiotic synergy via delayed lysis.** *Applied and environmental microbiology* 2018, **84:**e02085-02018.
14. Engeman E, Freyberger HR, Corey BW, Ward AM, He Y, Nikolich MP, Filippov AA, Tyner SD, Jacobs AC: **Synergistic killing and re-sensitization of Pseudomonas aeruginosa to antibiotics by phage-antibiotic combination treatment.** *Pharmaceuticals* 2021, **14:**184.
15. Carrigy NB, Larsen SE, Reese V, Pecor T, Harrison M, Kuehl PJ, Hatfull GF, Sauvageau D, Baldwin SL, Finlay WH: **Prophylaxis of Mycobacterium tuberculosis H37Rv infection in a preclinical mouse model via inhalation of nebulized bacteriophage D29.** *Antimicrobial agents and chemotherapy* 2019, **63:**10.1128/aac. 00871-00819.

16. Bavda VR, Jain V: **Deciphering the role of holin in mycobacteriophage D29 physiology.** *Frontiers in Microbiology* 2020, **11:**883.
17. Payne K, Sun Q, Sacchettini J, Hatfull GF: **Mycobacteriophage Lysin B is a novel mycolylarabinogalactan esterase.** *Molecular microbiology* 2009, **73:**367-381.
18. Payne KM, Hatfull GF: **Mycobacteriophage endolysins: diverse and modular enzymes with multiple catalytic activities.** *PLoS One* 2012, **7:**e34052.
19. Shariatinia Z: **Biopolymeric nanocomposites in drug delivery.** *Advanced Biopolymeric Systems for Drug Delivery* 2020**:**233-290.
20. Duncan MJ, Wheatley PS, Coghill EM, Vornholt SM, Warrender SJ, Megson IL, Morris RE: **Antibacterial efficacy from NO-releasing MOF–polymer films.** *Materials Advances* 2020, **1:**2509-2519.
21. Korany AH, Abouhmad A, Bakeer W, Essam T, Amin MA, Hatti-Kaul R, Dishisha T: **Comparative structural analysis of different mycobacteriophage-derived mycolylarabinogalactan esterases (Lysin B).** *Biomolecules* 2019, **10:**45.
22. Abouhmad A, Korany AH, Grey C, Dishisha T, Hatti-Kaul R: **Exploring the enzymatic and antibacterial activities of novel mycobacteriophage lysin B enzymes.** *International Journal of Molecular Sciences* 2020, **21:**3176.
23. Li Z, Peng Y, Xia X, Cao Z, Deng Y, Tang B: **Sr/PTA metal organic framework as a drug delivery system for osteoarthritis treatment.** *Scientific Reports* 2019, **9:**17570.
24. Ahmed SA, Nur Hasan M, Bagchi D, Altass HM, Morad M, Althagafi II, Hameed AM, Sayqal A, Khder AERS, Asghar BH: **Nano-MOFs as targeted drug delivery agents to combat antibiotic-resistant bacterial infections.** *Royal Society open science* 2020, **7:**200959.
25. Nguyen T-T-B, Chang H-C, Wu VW-K: **Adsorption and hydrolytic activity of lysozyme on diamond nanocrystallites.** *Diamond and related materials* 2007, **16:**872-876.
26. Subramaniam S, Thomas N, Gustafsson H, Jambhrunkar M, Kidd SP, Prestidge CA: **Rifampicin-loaded mesoporous silica nanoparticles for the treatment of intracellular infections.** *Antibiotics* 2019, **8:**39.
27. Kujur S, Singh A, Singh C: **Inhalation potential of rifampicin-loaded novel metal–organic frameworks for improved lung delivery: Physicochemical characterization, in vitro aerosolization and antimycobacterial studies.** *Journal of Aerosol Medicine and Pulmonary Drug Delivery* 2022, **35:**259-268.
28. Abouhmad A, Dishisha T, Amin MA, Hatti-Kaul R: **Immobilization to positively charged cellulose nanocrystals enhances the antibacterial activity and stability of hen egg white and T4 lysozyme.** *Biomacromolecules* 2017, **18:**1600-1608.
29. Ghosh R, Mondal S, Mukherjee D, Adhikari A, Ahmed SA, Alsantali RI, Khder AS, Altass HM, Moussa Z, Das R: **Oral drug delivery using a polymeric nanocarrier: Chitosan nanoparticles in the delivery of rifampicin.** *Materials Advances* 2022, **3:**4622-4628.

30. Aboutaleb E, Noori M, Gandomi N, Atyabi F, Fazeli MR, Jamalifar H, Dinarvand R: **Improved antimycobacterial activity of rifampin using solid lipid nanoparticles.** *International Nano Letters* 2012, **2:**1-8.
31. Amin BH, Abou-Dobara MI, Diab MA, Gomaa EA, El-Mogazy MA, El-Sonbati AZ, EL-Ghareib MS, Hussien MA, Salama HM: **Synthesis, characterization, and biological investigation of new mixed-ligand complexes.** *Applied Organometallic Chemistry* 2020, **34:**e5689.
32. Sherif MM, Elshikh HH, Abdel-Aziz MM, Elaasser MM, Yosri M: **In Vitro Antibacterial and Phytochemical Screening of Hypericum perforatum Extract as Potential Antimicrobial Agents against Multi-Drug-Resistant (MDR) Strains of Clinical Origin.** *BioMed Research International* 2023, **2023**.
33. Jarai BM, Stillman Z, Attia L, Decker GE, Bloch ED, Fromen CA: **Evaluating UiO-66 metal–organic framework nanoparticles as acid-sensitive carriers for pulmonary drug delivery applications.** *ACS applied materials & interfaces* 2020, **12:**38989-39004.
34. Zhou Y, Niu B, Wu B, Luo S, Fu J, Zhao Y, Quan G, Pan X, Wu C: **A homogenous nanoporous pulmonary drug delivery system based on metal-organic frameworks with fine aerosolization performance and good compatibility.** *Acta Pharmaceutica Sinica B* 2020, **10:**2404-2416.
35. Suvarna KS, Layton C, Bancroft JD: *Bancroft's theory and practice of histological techniques.* Elsevier health sciences; 2018.
36. Khadka P, Sinha S, Tucker IG, Dummer J, Hill PC, Katare R, Das SC: **Studies on the safety and the tissue distribution of inhaled high-dose amorphous and crystalline rifampicin in a rat model.** *International Journal of Pharmaceutics* 2021, **597:**120345.
37. Chokshi NV, Rawal S, Solanki D, Gajjar S, Bora V, Patel BM, Patel MM: **Fabrication and characterization of surface engineered rifampicin loaded lipid nanoparticulate systems for the potential treatment of tuberculosis: an in vitro and in vivo evaluation.** *Journal of Pharmaceutical Sciences* 2021, **110:**2221-2232.
38. Burley SK, Berman HM, Kleywegt GJ, Markley JL, Nakamura H, Velankar S: **Protein Data Bank (PDB): the single global macromolecular structure archive.** *Protein crystallography: methods and protocols* 2017**:**627-641.
39. Farboudi A, Mahboobnia K, Chogan F, Karimi M, Askari A, Banihashem S, Davaran S, Irani M: **UiO-66 metal organic framework nanoparticles loaded carboxymethyl chitosan/poly ethylene oxide/polyurethane core-shell nanofibers for controlled release of doxorubicin and folic acid.** *International journal of biological macromolecules* 2020, **150:**178-188.
40. Chen C, Chen D, Xie S, Quan H, Luo X, Guo L: **Adsorption behaviors of organic micropollutants on zirconium metal–organic framework UiO-66: analysis of surface interactions.** *ACS applied materials & interfaces* 2017, **9:**41043-41054.
41. Silva P, Vilela SM, Tome JP, Paz FAA: **Multifunctional metal–organic frameworks: from academia to industrial applications.** *Chemical Society Reviews* 2015, **44:**6774-6803.
42. Lv G, Liu J, Xiong Z, Zhang Z, Guan Z: **Selectivity adsorptive mechanism of different nitrophenols on UiO-66 and UiO-66-NH2 in aqueous solution.** *Journal of Chemical & Engineering Data* 2016, **61:**3868-

3876.

43. Shangkum GY, Chammingkwan P, Trinh DX, Taniike T: **Design of a semi-continuous selective layer based on deposition of UiO-66 nanoparticles for nanofiltration.** *Membranes* 2018, **8:**129.
44. Xu W, Dong M, Di L, Zhang X: **A facile method for preparing UiO-66 encapsulated Ru catalyst and its application in plasma-assisted CO2 methanation.** *Nanomaterials* 2019, **9:**1432.
45. Wang YL, Zhang S, Zhao YF, Bedia J, Rodriguez JJ, Belver C: **UiO-66-based metal organic frameworks for the photodegradation of acetaminophen under simulated solar irradiation.** *Journal of Environmental Chemical Engineering* 2021, **9:**106087.
46. Prabhu P, Fernandes T, Chaubey P, Sawarkar S: **Design, development and characterization of carrier mediated drug delivery system for effective management of Osteoarticular Tuberculosis.** 2021.
47. Abdelmoaty AS, El-Wakeel ST, Fathy N, Hanna AA: **High Performance of UiO-66 Metal–Organic Framework Modified with Melamine for Uptaking of Lead and Cadmium from Aqueous Solutions.** *Journal of Inorganic and Organometallic Polymers and Materials* 2022, **32:**2557-2567.
48. Yang Q, Zhang HY, Wang L, Zhang Y, Zhao J: **Ru/UiO-66 Catalyst for the Reduction of Nitroarenes and Tandem Reaction of Alcohol Oxidation/Knoevenagel Condensation.** *ACS Omega* 2018, **3:**4199-4212.
49. Li Z, Zhao S, Wang H, Peng Y, Tan Z, Tang B: **Functional groups influence and mechanism research of UiO-66-type metal-organic frameworks for ketoprofen delivery.** *Colloids Surf B Biointerfaces* 2019, **178:**1-7.
50. Gholami M, Hekmat A, Khazaei M, Darroudi M: **OXA-CuS@UiO-66-NH(2) as a drug delivery system for Oxaliplatin to colorectal cancer cells.** *J Mater Sci Mater Med* 2022, **33:**26.
51. Nasrabadi MRB, Ghasemzadeh MA, Zand Monfared MR: **The preparation and characterization of UiO-66 metal–organic frameworks for the delivery of the drug ciprofloxacin and an evaluation of their antibacterial activities.** *New Journal of Chemistry* 2019.
52. Jing C, Bizhu S, Chenrui S, Panliang Z, Weifeng X, Yu L, Biquan X, Kewen T: **Immobilization of lipase AYS on UiO-66-NH2 metal-organic framework nanoparticles as a recyclable biocatalyst for ester hydrolysis and kinetic resolution.** *Separation and Purification Technology* 2020, **251:**117398.
53. Negar M-K, Seyed Abbas S, Ali M: **In situ synthesis of a drug-loaded MOF at room temperature.** *Microporous and Mesoporous Materials* 2014, **186:**73-79.
54. Ibrahim AH, El-Mehalmey WA, Haikal RR, Safy MEA, Amin M, Shatla HR, Karakalos SG, Alkordi MH: **Tuning the Chemical Environment within the UiO-66-NH(2) Nanocages for Charge-Dependent Contaminant Uptake and Selectivity.** *Inorg Chem* 2019, **58:**15078-15087.
55. Alves Júnior J, Baldo J: **The Behavior of Zeta Potential of Silica Suspensions.** *New Journal of Glass and Ceramics* 2014, **04:**29-37.
56. Albayati N, Kadhom M: **Preparation of functionalised UiO-66 metal–organic frameworks (MOFs) nanoparticles using deep eutectic solvents as a benign medium.** *Micro & Nano Letters* 2020, **15**.

57. Kujur S, Singh A, Singh C: **Inhalation Potential of Rifampicin-Loaded Novel Metal–Organic Frameworks for Improved Lung Delivery: Physicochemical Characterization, In Vitro Aerosolization and Antimycobacterial Studies.** *Journal of Aerosol Medicine and Pulmonary Drug Delivery* 2022, **35**.
58. Ragusa J, Gonzalez D, Li S, Noriega S, Skotak M, Larsen G: **Glucosamine/L-lactide copolymers as potential carriers for the development of a sustained rifampicin release system using Mycobacterium smegmatis as a tuberculosis model.** *Heliyon* 2019, **5:**e01539.
59. Carneiro S, Carvalho K, Aguiar-Soares R, Carneiro C, Andrade M, Duarte R, Santos O: **Functionalized rifampicin-loaded nanostructured lipid carriers enhance macrophages uptake and antimycobacterial activity.** *Colloids and Surfaces B: Biointerfaces* 2018, **175**.
60. Yunus Basha R, Kumar TS, Doble M: **Dual delivery of tuberculosis drugs via cyclodextrin conjugated curdlan nanoparticles to infected macrophages.** *Carbohydrate Polymers* 2019, **218**.
61. Mistry N, Bandyopadhyaya R, Mehra S: **ZnO Nanoparticles and Rifampicin Synergistically Damage the Membrane of Mycobacteria.** *ACS Applied Nano Materials* 2020, **4:**3174–3184
62. Mistry N, Bandyopadhyaya R, Mehra S: **Enhancement of Antimycobacterial Activity of Rifampicin Using Mannose-Anchored Lipid Nanoparticles against Intramacrophage Mycobacteria.** *ACS Appl Bio Mater* 2022, **5:**5779-5789.
63. Elbasuney S, Yehia M, Ismael S, Al-Hazmi N, El-Sayyad G, Tantawy H: **Potential Impact of Reduced Graphene Oxide Incorporated Metal Oxide Nanocomposites as Antimicrobial, and Antibiofilm Agents Against Pathogenic Microbes: Bacterial Protein Leakage Reaction Mechanism.** *Journal of Cluster Science* 2022, **34**.
64. Varma A, Warghane A, Dhiman N, Paserkar N, Upadhye V, Modi A, Saini R: **The role of nanocomposites against biofilm infections in humans.** *Frontiers in Cellular and Infection Microbiology* 2023, **13:**1104615.
65. Bhardwaj N, Pandey S, Mehta J, Bhardwaj S, Kim K-H, Deep A: **Bioactive Nano Metal-Organic Frameworks as Antimicrobials Against Gram-Positive and Gram-Negative Bacteria.** *Toxicology Research* 2018, **7**.
66. Díez-Pascual AM, Luceño-Sánchez JA: **Antibacterial Activity of Polymer Nanocomposites Incorporating Graphene and Its Derivatives: A State of Art.** *Polymers* 2021, **13:**2105.
67. Zeynali kelishomi F, Khanjani S, Fardsanei F, Saghi Sarabi H, Nikkhahi F, Dehghani B: **Bacteriophages of Mycobacterium tuberculosis, their diversity, and potential therapeutic uses: a review.** *BMC Infectious Diseases* 2022, **22:**957.
68. Brar A, Majumder S, Navarro MZ, Benoit-Biancamano M-O, Ronholm J, George S: **Nanoparticle-Enabled Combination Therapy Showed Superior Activity against Multi-Drug Resistant Bacterial Pathogens in Comparison to Free Drugs.** *Nanomaterials* 2022, **12:**2179.
69. Okuda T, Morishita M, Mizutani K, Shibayama A, Okazaki M, Okamoto H: **Development of spray-freeze-dried siRNA/PEI powder for inhalation with high aerosol performance and strong pulmonary gene silencing activity.** *Journal of Controlled Release* 2018, **279**.

70. Ramappa V, Aithal GP: **Hepatotoxicity Related to Anti-tuberculosis Drugs: Mechanisms and Management.** *J Clin Exp Hepatol* 2013, **3:**37-49.
71. Garcia-Contreras L, Sung J, Ibrahim M, Elbert K, Edwards D, Hickey T: **Pharmacokinetics of Inhaled Rifampicin Porous Particles for Tuberculosis Treatment: Insight into Rifampicin Absorption from the Lungs of Guinea Pigs.** *Molecular pharmaceutics* 2015, **12**.
72. Singh C, Koduri LV, Dhavale V, Bhatt T, Kumar R, Grover V, Tikoo K, Sarasija S: **Potential of aerosolized rifampicin lipospheres for modulation of pulmonary pharmacokinetics and bio-distribution.** *International Journal of Pharmaceutics* 2015, **495**.
73. Jarai B, Stillman Z, Attia L, Decker G, Bloch E, Fromen C: **Evaluating UiO-66 Metal-Organic Framework (MOF) Nanoparticles as Acid-Sensitive Carriers for Pulmonary Drug Delivery Applications.** *ACS Applied Materials & Interfaces* 2020, **35:**38989–39004
74. Chunbai H, Yiping H, Lichen Y, Cui T, Chunhua Y: **Effects of particle size and surface charge on cellular uptake and biodistribution of polymeric nanoparticles.** *Biomaterials* 2010, **31:**3657-3666.

Figures

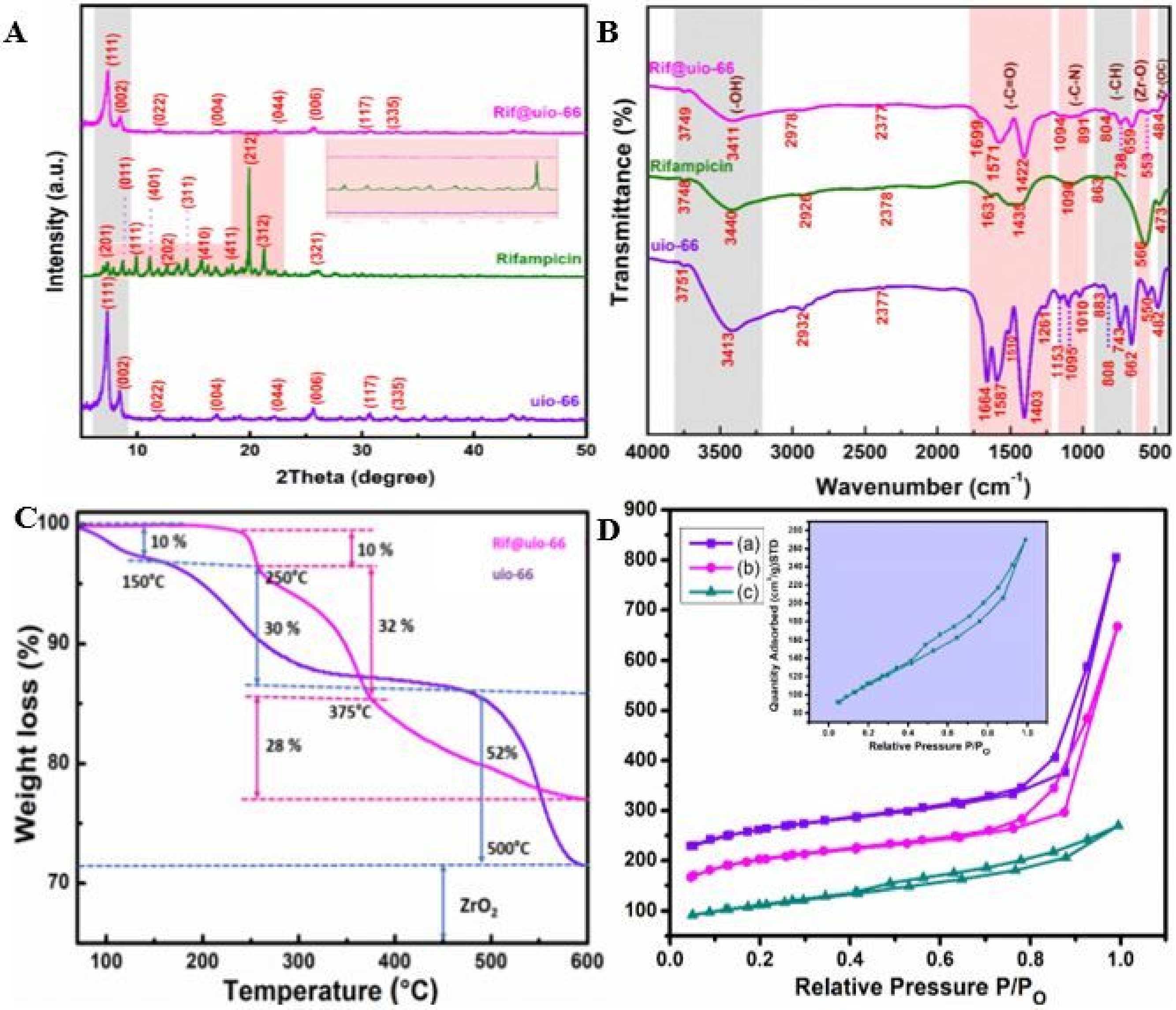

Figure 1

(A) X-ray diffraction patterns, Inset from *2q* scale within 5-20 **(B)** FTIR spectra (**C)** TGA curves and **(D)** Nitrogen adsorption−desorption isotherms at 77K of **(a)**UiO-66 **(b)** Rif@UiO-66, and (**c**) LysB/Rif@UiO-66. (inset)

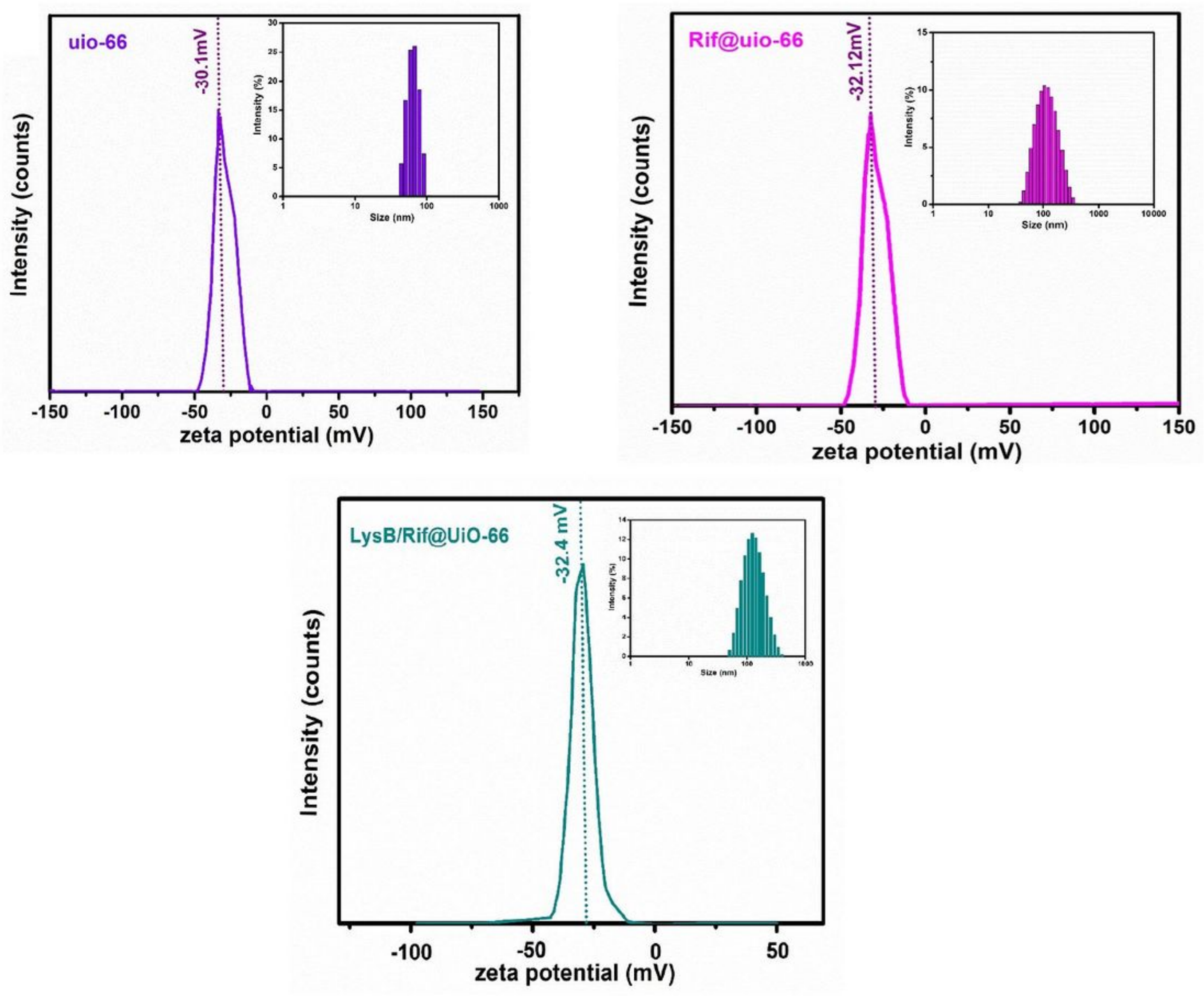

Figure 2

Zeta potential measurements and (inset) DLS distribution for UiO-66, Rif@UiO-66, and LysB/Rif@UiO-66.

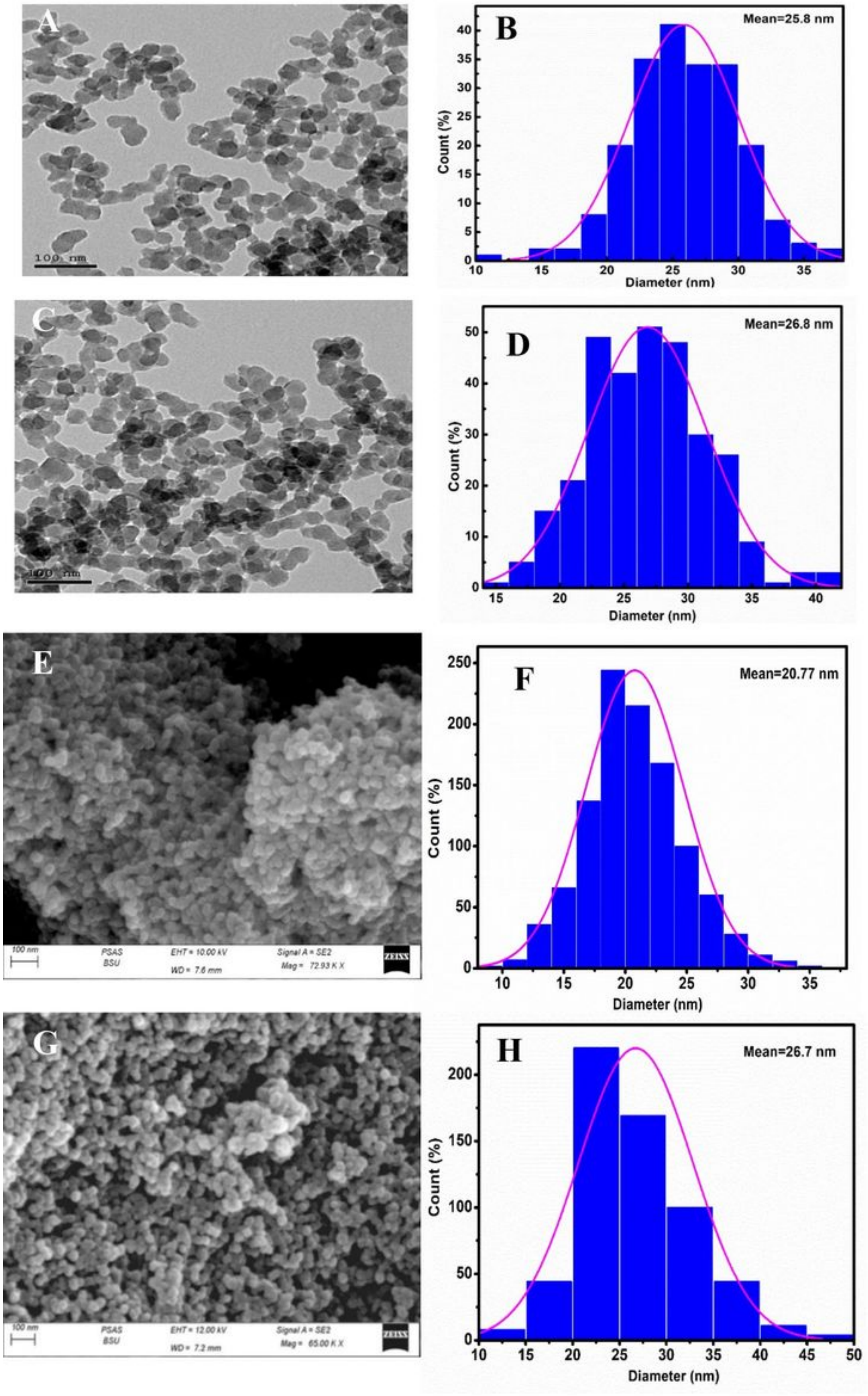

Figure 3

HRTEM, FE-SEM micrographs and particle size distributions of **(A, B, E and F)** UiO-66 and **(C, D, G and H)** Rif@UiO-66

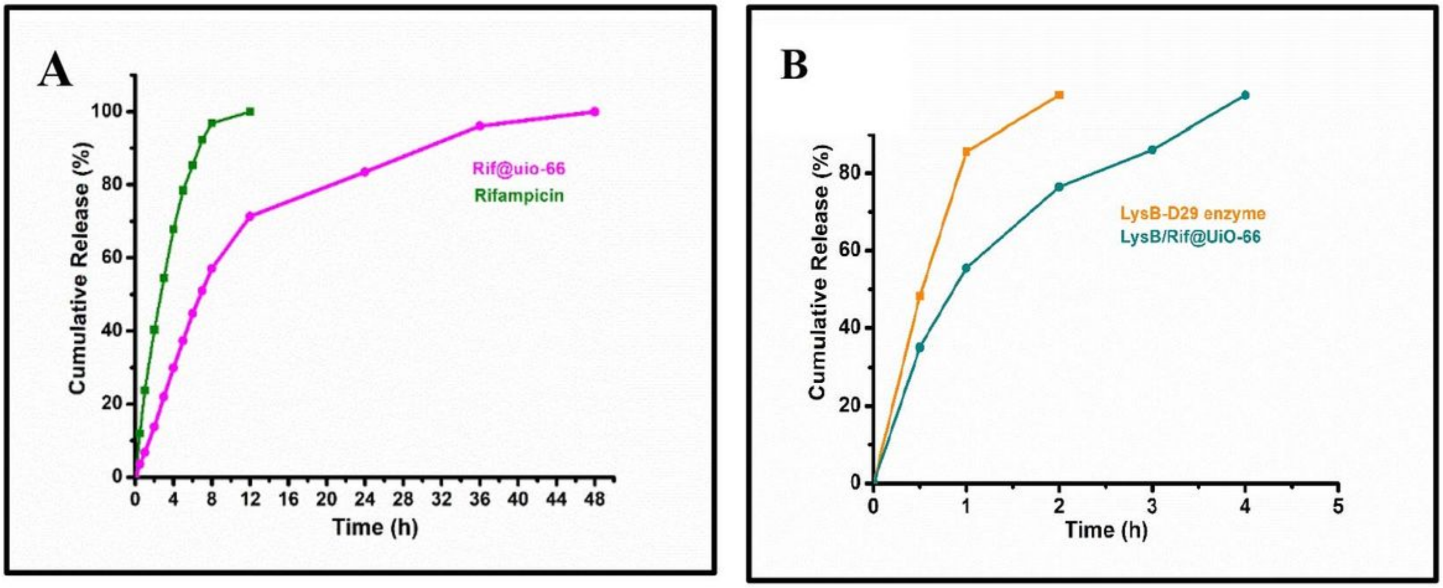

Figure 4

(**A**) In vitro rifampicin release curve from Rif@UiO-66 and free Rif and (**B**) In vitro lysine B release curve from LysB/Rif@UiO-66 and free LysB at the same condition.

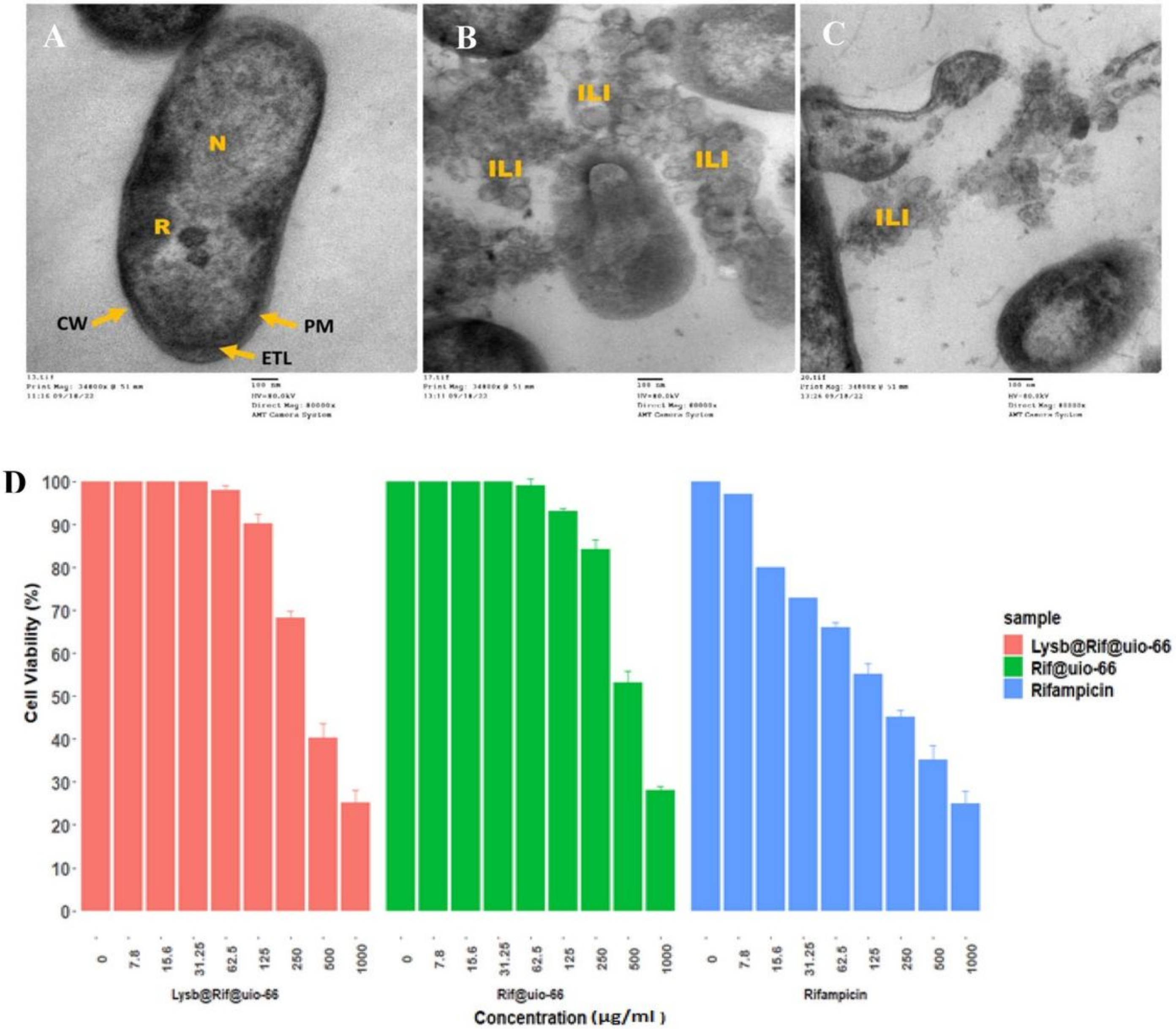

Figure 5

TEM micrographs showing the ultrastructure of Mycobacterium smegmatis**;** **(A)** control, **(B)** affected with LysB/Rif@UiO-66, **(C)** affected with Rifampicin. Scale Bar = 100 nm. X = 80000, and **(D)** Relative cell viabilities of mammalian cells from African Green Monkey Lung (Vero) cell after incubated with various concentration of Rifampicin, Rif@uio-66 and LysB/Rif@UiO-66 for 48 h (data are expressed as mean ± SD, n = 3).

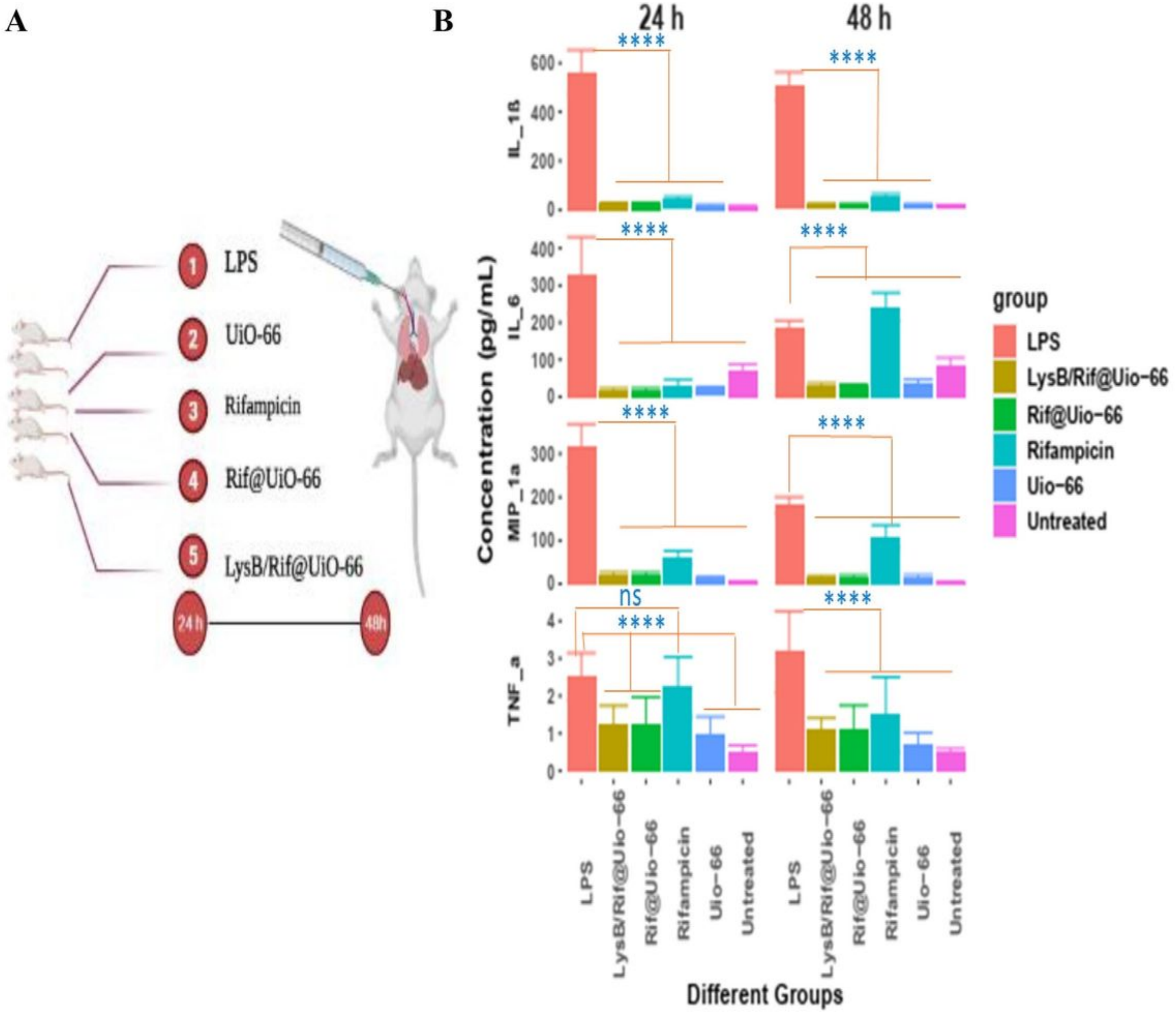

Figure 6

Experimental procedures for invivo toxicity and inflammatory effects of LPS,UiO-66, Free Rif,Rif@UiO-66 and LysB/Rif@UiO-66 at 24h and 48h.Created by BioRender.com. **(B)** Concentrations of inflammatory cytokines in BALF of rats after pulmonary delivery of different samples for 24 and 48 h (data are expressed as mean ± SD, n = 5). Significant difference is regarded as **** P ≤ 0.0001, ns not significant compared to LPS.

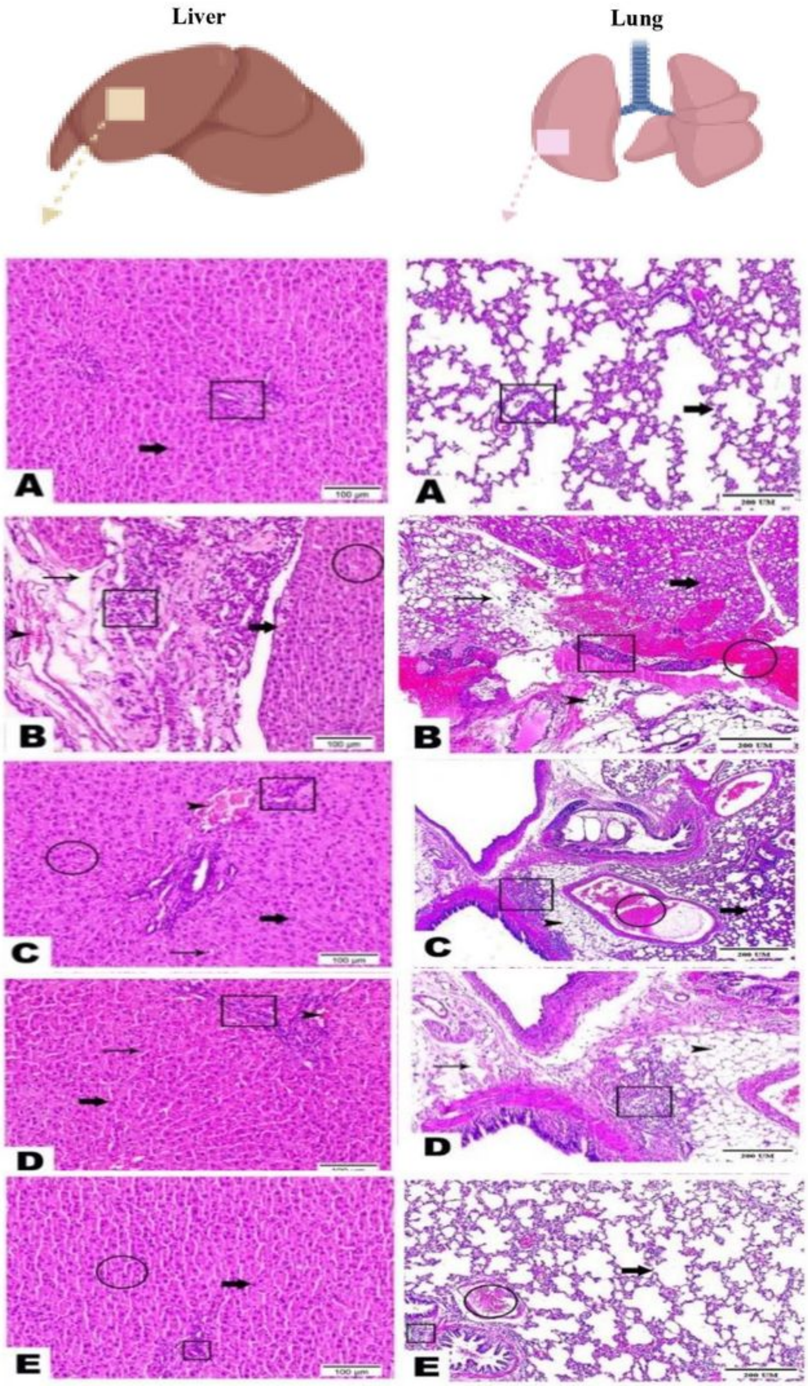

Figure 7

Photomicrographs of Hematoxylin- and eosin-stained liver sections (Magnification power = 200 X and scale bar = 100 µm) and lung sections Magnification power = 100 X and scale bar = 200 µm). of the negative control group **(A)**, Rif-treated group **(B),** UiO-66 treated group **(C);** Rif@UiO-66 treated group **(D),** and LysB/Rif@ UiO-66**(E)**.

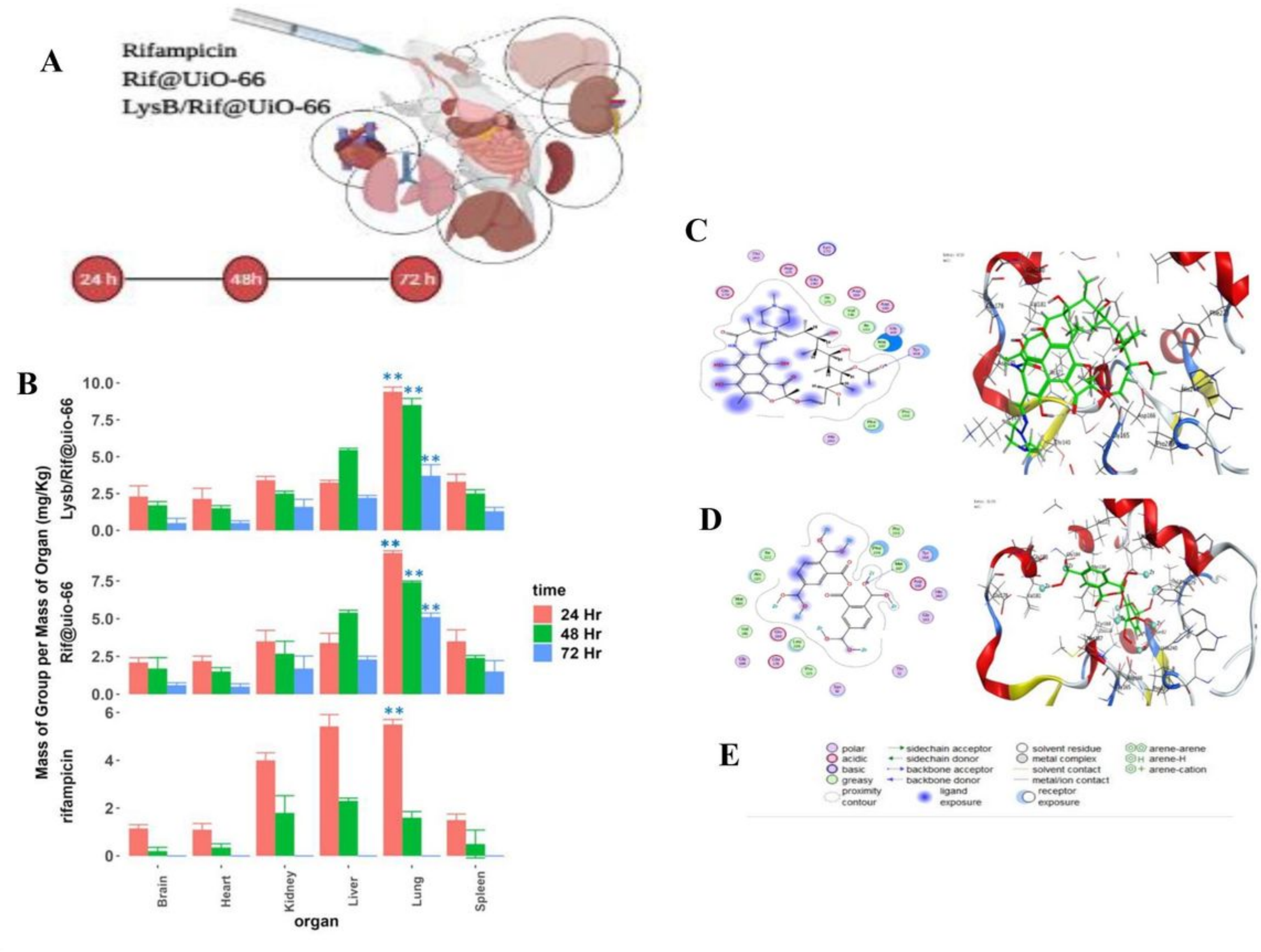

Figure 8

(A) Experimental procedures for invivo biodistrubition of LPS, UiO-66, Free Rif,Rif@UiO-66 and LysB/Rif@UiO-66 at24h, 48h and 72h. Created by BioRender.com.**(B)** Biodistribution profile of pure Rif, Rif@UiO-66 and LysB/ Rif@UiO-66 in various organs at 24 h, 48 h, and 72 h (mean ± SD, n=5) (**$p < 0.01$), and 2D and 3D diagrams show the interaction between **(C)** Rifampicin and active sites of 3HC7 protein, **(D)** UiO-66 and active sites of 3HC7 protein, and **(E)** The representative key for the types of interaction between Compounds and protein receptors.

Supplementary Files

This is a list of supplementary files associated with this preprint. Click to download.

- supplemntrydata.docx